Published in final edited form as:
Magn Reson Med. 2013 November ; 70(5): 1460–1469. doi:10.1002/mrm.24563.

Error Model for Reduction of Cardiac and Respiratory Motion Effects in Quantitative Liver DW-MRI

Paul Murphy, MD PhD[1,+], **Tanya Wolfson, MA**[2], **Anthony Gamst, PhD**[2], **Claude Sirlin, MD**[1], and **Mark Bydder, PhD**[1]

[1]Department of Radiology, University of California – San Diego, 200 West Arbor Drive, San Diego, CA 92103-0834

[2]Computational and Applied Statistics Laboratory SDSC, University of California – San Diego

Abstract

Diffusion-weighted images of the liver exhibit signal dropout from cardiac and respiratory motion, particularly in the left lobe. These artifacts cause bias and variance in derived parameters that quantify intra-voxel incoherent motion (IVIM). Many models of diffusion have been proposed, but few separate attenuation from diffusion or perfusion from that of bulk motion. The error model proposed here (Beta*LogNormal) is intended to accomplish that separation by modeling stochastic attenuation from bulk motion as multiplication by a Beta-distributed random variate. Maximum likelihood estimation with this error model can be used to derive IVIM parameters separate from signal dropout, and does not require *a priori* specification of parameters to do so. Liver IVIM parameters were derived for six healthy subjects under this error model and compared with least-squares estimates. Least-squares estimates exhibited bias due to cardiac and respiratory gating and due to location within the liver. Bias from these factors was significantly reduced under the Beta*LogNormal model, as was within-organ parameter variance. Similar effects were appreciable in diffusivity maps in two patients with focal liver lesions. These results suggest that, relative to least-squares estimation, the Beta*LogNormal model accomplishes the intended reduction of bias and variance from bulk motion in liver diffusion imaging.

Introduction

Quantitative measures derived from diffusion MR images can aid in the diagnosis of focal and diffuse liver diseases (1). Diffusion images are analyzed by modeling signal attenuation as a function of b-value (2; 3). Many organs exhibit mono-exponential attenuation, which is quantified with a single apparent diffusion coefficient (ADC). Liver ADC's have been widely reported (4–9). Liver actually exhibits bi-exponential attenuation (10; 11), which is quantified, under intra-voxel incoherent motion (IVIM) theory (12), with three parameters: a diffusion coefficient (D), a pseudo-diffusion coefficient (D*) reflecting attenuation of perfusion (in liver, this number is typically an order of magnitude greater than the diffusivity of bulk water at 37°C), and a fraction (F) reflecting the proportion of signal from perfusing spins at b=0. Among focal liver lesions, malignancies generally exhibit low ADC and D,

[+]Corresponding author: paul.martin.murphy@gmail.com.

reflecting restricted diffusion, while benign lesions such as cysts and hemangiomas have high ADC and D (4; 13). Cirrhotic liver generally has lower ADC, D*, D, and F relative to normal liver (14–17). However, poor reproducibility of these quantities remains a barrier to widespread clinical adoption of quantitative diffusion imaging in liver (1). Reducing the bias and variance in measurements of IVIM parameters may help address this problem.

Cardiac and respiratory motion are known sources of bias and variance in diffusion imaging, due to the exquisite motion sensitivity conferred by strong diffusion weighting (5–7; 9; 18–20). Bulk motion from these physiologic processes causes signal dropout in single shot diffusion-weighted images (Fig 1). This artifact occurs at specific times in the cardiac and respiratory cycles, but affects random images acquired during untriggered, free-breathing, diffusion-weighted sequences. The left lobe of the liver is especially, but not exclusively, affected due to its proximity to the point of maximal impact of the heart (5; 18). Signal dropout from bulk motion mimics signal attenuation from diffusion and perfusion, leading to upward bias and increased variance of ADC and IVIM parameters. In previous studies, liver ADC's measured with prospective cardiac triggering had greater mean and standard deviation during systole than during diastole (5; 6). Liver ADC's measured during free-breathing were greater than (20) or equal to (7) those measured during breath-holding. Liver ADC's measured with prospective respiratory triggering were greater than (7; 21) or equal to (9) those measured during breath-holding. Respiratory triggering with a navigator technique did reduce the standard deviation of ADC relative to breath-holding in one study (21). Overall, these studies demonstrate that prospective triggering and breath-holding mitigate the effects of bulk motion on ADC measurement. However, these physiologic methods limit the efficiency of image acquisition, since artifact-prone times in the cardiac and respiratory cycles must be avoided. This is problematic when a large number of images are required, for example, to acquire multiple b-values for IVIM parameter determination, or to acquire multiple repetitions for increased SNR.

For this study, we developed a method to mitigate bulk motion artifacts that is based on a reconsideration of the statistical distribution of errors in diffusion images. IVIM parameters are often derived by minimizing the sum-of-squared error between measured and predicted signal magnitudes (18). This process is known as least-squares (LS) fitting, and is equivalent to maximum likelihood estimation under an error model in which signal magnitudes are assumed to be normally distributed. The validity of that assumption is questionable. Although the normal distribution closely approximates many of the magnitude distributions for different coils and reconstructions at high signal-to-noise ratio, those distributions are derived by assuming normal error in the real and imaginary parts (ie, the cartesian coordinates) of the complex signal (22). Bulk motion in the presence of a gradient causes, instead, phase shifts of individual spins (23) (Fig 2). For this reason, it is more appropriate to express errors from this mechanism in terms of the magnitude and phase (ie, the polar coordinates) of the complex signal. The Beta*LogNormal (BLN) error model is a statistical distribution for signal magnitude derived from one set of assumptions about the phase errors of individual spins. We propose using it in place of LS fitting for maximum likelihood estimation of IVIM parameters from magnitude diffusion-weighted images. This error model is distinct from other models of diffusion (2; 3), because it separates attenuation from

diffusion and perfusion from that of bulk motion. In contrast to other approaches (18; 24), this method does not require *a priori* parameter specification to do so.

In this study, we compare IVIM parameters derived from the BLN error model with those derived from the LS error model. Direct assessment of the accuracy of parameters derived from each model is not possible, since perfusion does not occur in *ex vivo* liver phantoms that could otherwise be used as gold standard reference values (25). However, the effects of bulk motion vary across the cardiac and respiratory cycles and across the liver. Therefore, bias from bulk motion can be assessed on the basis of change between different varieties of cardiac and respiratory gating, and on the basis of differences between left and right liver lobes. Within-organ variance reveals another aspect of the precision of measurements with each error model. The purpose of this study is to test the hypothesis that IVIM parameters have lower bias and variance from bulk motion when estimated with the BLN error model than when estimated with the LS error model.

Theory

The IVIM theory of diffusion (12) proposes that, in the presence of intra-voxel perfusion, attenuation will follow a bi-exponential:

$$Y_i = Y_0 \left(F \cdot e^{-b_i D^*} + (1-F) \cdot e^{-b_i D} \right) \quad [1]$$

The parameters of this equation are: the signal magnitude (Y), the b-value (b), and D, D* and F, as defined above. These parameters are often estimated by least squares (LS) fitting, under an implicit assumption of normally distributed error:

$$Y_i \sim Normal \left(\mu_i, \sigma^2 \right) \quad [2]$$

$$\mu_i = Y_0 \left(F \cdot e^{-b_i D^*} + (1-F) \cdot e^{-b_i D} \right) \quad [3]$$

The parameters of [Eq 2] are the mean and variance of the normal distribution (μ and σ^2). Two major objections to this assumption can be raised. First, diffusion images have properties that cannot be represented by a normal distribution, such as non-negative signal, and negatively skewed errors. Other distributions for signal magnitude, such as the Rician or noncentral chi-squared distributions, capture the former but not the latter property.

Second, [Eq 2] and [Eq 3] do not capture the fact that bulk motion artifacts arise from a separate physical mechanism than diffusion and pseudo-diffusion, with a separate effect on signal magnitude. Bipolar gradients used for diffusion weighting also give rise to phase from the linear motion of individual spins, as in phase contrast angiography, where:

$$\phi = (\gamma \Delta \delta) \vec{G}_i \cdot \vec{v} \quad [4]$$

The parameters of this equation are the gyromagnetic ratio (γ), the pulse width (δ) and separation (Δ), the gradient strength (G), and the velocity of motion (v). The velocity of bulk motion for spins within a voxel may vary in magnitude, since soft tissue is deformable, or in direction, since it may emanate radially from the point of maximal impact of the heart (Fig 2). Either phenomenon will cause phase dispersion through [Eq 4]. This residual phase gradient induced by voxel deformation will cause magnitude attenuation by a factor between zero and one. The functional form of such attenuation under certain assumptions is given in (12). Attenuation from bulk motion can be empirically observed (Fig 1e & f), and will be conflated with the effects of diffusion and perfusion under [Eq 2] and [Eq 3].

We propose an error model in which stochastic attenuation from bulk motion is represented as a term separate from diffusion and perfusion. In this model, signal magnitude is distributed as a LogNormal random variate, related only to IVIM diffusion parameters, multiplied by an independent Beta random variate, related only to bulk motion:

$$Y_i \sim Beta(\alpha, 1) \cdot e^{Normal(\mu_i, \sigma^2)} \quad [5]$$

$$\mu_i = log\left(Y_0\left(F \cdot e^{-b_i D^*} + (1-F) \cdot e^{-b_i D}\right)\right) \quad [6]$$

We refer to this as the Beta*LogNormal (BLN) error model or distribution (Fig 3). The parameters of [Eq 5] are the mean and variance of the LogNormal distribution (μ and σ^2), and α. Beta random variates range continuously between zero and one depending on the parameter α. Multiplication by a Beta random variate represents stochastic attenuation between zero and the signal maximum. A higher value of α in a voxel corresponds with a higher probability of acquiring an image unaffected by signal dropout in that voxel. The Beta form can be derived from an assumption about the distribution of the bulk motion-induced phase of spins within a voxel over imaging time (see Appendix). The LogNormal form is chosen to allow for maximum likelihood estimation with a closed-form probability density function, a considerable computational advantage for parametric map generation. With sufficiently high signal-to-noise ratio, the BLN error model can be used in place of other distributions for signal magnitude, such as the normal, Rician, or noncentral chi-squared. In contrast to these distributions, signal dropout can be captured by the α parameter of the BLN distribution without affecting estimates of the IVIM parameters.

Methods

Subjects

Approval for human MR imaging was obtained from the local IRB board. A prospective, observational, single site study was initiated. Six healthy volunteers (5 males and 1 female, ages 23–46 years old) were recruited. Two patients with focal liver lesions (1 male and 1 female, ages 67 and 64 years old) were also recruited.

Imaging technique

Diffusion-weighted spin-echo echo-planar-imaging was performed using a 3T GE Signa Excite MR scanner using the following scan parameters: TE: 61.6 ms, TR: 3500 ms, FOV: 40 cm × 40 cm, matrix size: 64 × 64 and (in an additional scan of volunteers) 92 × 92, k-space acquisition: 100%, ASSET factor: 2, coil: 8-channel torso coil, fat suppression: SPECIAL, slice direction: axial, number of slices: 10, slice thickness: 10 mm, slice spacing 2.5 mm. Slices were chosen to span the entirety of the liver and to include the upper pole of each kidney. For volunteers, the following b-values were acquired: 0, 10, 20, 30, 50, 75, 100, 200, 300, 400, 500, using a single gradient direction (3n1). All b-values are given in units of [s/mm^2]. Multiple single shot (NEX 1) images were acquired at each b-value: 4 repeats for b < 100, 24 repeats for b >= 100. For patients, the following b-values were acquired: 0, 10, 20, 30, 50, 75, 100, 200, 300, 400, 500, 600, 700, 800, with 4 repeats for b < 100 and 16 repeats for b >= 100. The temporal order of b-value acquisition was randomized (for example: 10, 500, 200, 30, 10, 40, 200, …). Subjects were instructed to breathe freely during the course of the exam. A peripheral pulse plethysmography monitor was placed on the subject's right 2nd finger and a respiratory bellows monitor was placed around the subject's abdomen. Image acquisition was not prospectively triggered. The timing of cardiac and respiratory triggers during imaging was recorded for subsequent retrospective gating. The timing of the excitation pulse of each image was recorded as well. Total scan time was approximately 9 minutes per subject.

Definititions and criteria

The *retrospective trigger delay*, defined as the time between the excitation pulse of each image and the immediately preceding cardiac or respiratory trigger, was calculated with in-house software. The *cardiac or respiratory cycle fraction*, defined as the retrospective trigger delay divided by the time interval between immediately preceding and subsequent triggers (similar to (23)), was also calculated for each image. Retrospective gating was performed by filtering images to cycle fractions between 0.50–0.75 for cardiac diastole, and 0.20–0.60 for respiratory quiescence, or both. These specific gating thresholds were chosen on the basis of triggering values from the literature (5) and visual inspection of graphs such as (Fig 1c & d).

Parameter estimation

In-house software was used to generate maps of maximum likelihood estimates of each IVIM parameter under the LS and BLN error models. The Levenberg-Marquardt algorithm (Wuttke J, lmfit version 3.2, http://www.messen-und-deuten.de/lmfit/) was used for LS estimation of Y_0, D, and F of [Eq 1]. Simplex minimization (26) was used for estimation of Y_0, D, F and α of [Eq. 4] under the BLN model. D* was held fixed at 70E-3 mm^2/s, on the basis of previously published results (27). In the BLN error model, α was not allowed to vary with b-value.

Image analysis

In the scans performed on volunteers, multiple ROI's were drawn in a magnitude-averaged b=0 image of every slice in the left (n=86) and right (n=164) lobes of the liver, as well as in

the kidneys (n=36), spleen (n=67), and the paraspinous muscles of the back (n=112). ROI's were drawn to avoid prominent vasculature, and were colocalized between scans performed at the 64 × 64 and 92 × 92 matrix sizes. The mean value of D and F over all voxels was calculated for each ROI for both error models.

Statistical analysis

Six tests were performed to compare IVIM parameter estimates from each error model. The first four tests were structured to evaluate the hypotheses that BLN estimates changed less than LS estimates as a function of factors associated with bulk motion, since mitigation of bulk motion artifacts was the intended effect of the BLN model. First, to test whether the estimates from the BLN error model were different than estimates from the LS error model, we used mixed effects linear regression, comparing IVIM parameters, using error model as the fixed effect. The random effects of this and all subsequent regressions were subject and ROI. Second, to test whether estimates from each error model changed as a function of gating, we used mixed effects linear regression, comparing IVIM parameters, using gating variant as the fixed effect. Third, to test whether BLN estimates changed less than LS estimates as a function of gating, we used mixed effects linear regression, comparing the magnitude of gating-dependent changes in IVIM parameters, using error model as the fixed effect. Fourth, to test whether differences between the left and right liver lobes were lower for BLN estimates than for LS estimates, we used mixed effects linear regression, comparing IVIM parameters, using error model and liver lobe as the fixed effects, with an interaction term. Fifth, to test whether differences between organ types were detected by each error model, we used mixed effects linear regression, comparing IVIM parameters in the right liver lobe with the left liver lobe, spleen, kidney, and muscle, using organ type as the fixed effect. Finally, to test whether the variance of BLN estimates was lower than the variance of LS estimates, we used the variance ratio test to compare the variance of IVIM parameters within each organ. Each of these six tests was performed using data from the 64 × 64 and 92 × 92 matrix sizes separately. Results from the 64 × 64 matrix size are reported below, results from the 92 × 92 matrix size are reported in the Supplemental Information. All statistical tests were performed using the R software package (R Foundation for Statistical Computing, 2009, http://www.R-project.org) using the nlme library (R Core team, nlme version 3.1-103, http://cran.r-project.org/web/packages/nlme/).

Results

IVIM parameter maps

Typical IVIM parameter maps derived from each error model, as well as map of α from the BLN error model, are shown for a volunteer in (Fig 4) and for two patients with focal liver lesions in (Fig 5).

Comparison of IVIM parameters between error models

The LS and BLN error models produced different estimates of D and F in all cases ($P<0.001$) (Table S1), with LS estimates being greater than BLN estimates.

Comparison of IVIM parameters across gating variants

LS estimates of D and F changed significantly with gating ($P<0.01$, except for one case where $P>0.1$). By contrast, BLN estimates of D did not change significantly with gating ($P>0.1$) (Fig 6). BLN estimates of F changed significantly with gating ($P<0.01$, except for two cases where $P>0.1$).

Comparison of gating-dependent changes between error models

Gating-dependent changes in D were significantly lower for BLN estimates than for LS estimates in all cases ($P<0.05$) (Fig 7, Table S1). Gating-dependent changes in F were not significantly different between BLN estimates and LS estimates ($P>0.1$, except for one case).

Comparison of lobe-dependent differences between error models

Differences in D and F between the right and left lobes were significantly lower for BLN estimates than for LS estimates ($P<0.001$) (Fig 7).

Comparison of IVIM parameters between organs

LS and BLN estimates of D and F in both lobes of liver and in spleen, kidney and paraspinous muscles of the back are given in (Table S2) and (Fig 8). There were significant differences between right liver lobe and all other organs for each parameter from both error models ($P<0.01$), except for BLN estimates of F when compared between right and left lobes of the liver ($P=0.28$).

Within-organ variance of IVIM parameters

The within-organ variance of BLN estimates of D was significantly lower than the variance of LS estimates of D ($P<0.05$) in right lobe of liver, spleen and kidney. In left lobe of liver and back, variance of D was lower for BLN estimates, but not significantly ($P=0.12$ and $P=0.62$).

Discussion

The primary results of this study were that estimates of diffusivity (D) changed significantly less as a function of gating and liver lobe when derived with the BLN model than with the LS model. Estimates of perfusion fraction (F) changed significantly less as a function of lobe when derived with the BLN model than with the LS model. Differences in D and F between organ types were significant with both error models, as expected. However, the within-organ variance of estimates of D was significantly smaller with the BLN model than with the LS model, except in left liver lobe and in muscle, where variances were not significantly different. Results were similar at two different matrix sizes (see Supplemental Information). Similar effects were appreciable in diffusivity maps in two patients with focal liver lesions (Fig 5).

Under the assumption that diffusion compartment sizes do not change during the cardiac or respiratory cycles or between different locations in healthy liver, gating- and lobe-dependent changes in IVIM parameters are a reflection of bias in the measurement technique. By that

assessment, BLN estimates of diffusivity and perfusion fraction were less biased than LS estimates. Within-organ variance of diffusivity was lower for BLN estimates as well. Such invariance could indicate a reduction in sensitivity to true effects. However, differences between organ types were significant for both error models, suggesting that sensitivity to true effects is preserved. With its sensitivity to true effects and its relative invariance to known confounders, the BLN error model is likely to improve the reproducibility of IVIM parameter measurement.

In previous studies, estimates of liver ADC were generally lower during diastole than during systole, and lower during breath-holding than during free-breathing or respiratory triggered scans. This likely reflects positive bias from cardiac and respiratory motion. Our results are consistent with these expectations in two ways. First, retrospective gating to quiescent phases of the cardiac and respiratory cycles generally reduced LS estimates of both D and F, consistent with reduction in bias through gating. Second, BLN estimates of D and F were generally lower than LS estimates, consistent with reduction in bias through use of the BLN error model.

BLN estimation has advantages over physiologic methods for mitigating the effects of bulk motion on diffusion parameters. Breath-holding limits the number of images that can be acquired. Retrospective gating and prospective triggering, from either navigators or monitors, limit the rate of image acquisition. For instance, the thresholds used for combined cardiac and respiratory gating in this paper resulted in using approximately 10% of acquired images for parameter derivation. The BLN error model can utilize all of the images acquired during an untriggered, free-breathing scan. To do so, it must estimate an extra parameter a from the data to quantify the degree of signal dropout in each voxel. This presents a trade-off between the amount of data used in each approach and the number of parameters derived from it. However, that trade-off favors using the BLN model in untriggered, free-breathing scans, since it allows the use of 10 times more data (relative to gating using the same amount of scan time) at the cost of estimating only a single extra parameter. An important implication for clinical sequences is that repeated single shot images must be obtained, since a can only be estimated from the distribution of signal intensity, which is lost by averaging over multiple excitations. Inferring this parameter from the data constitutes an advantage of the BLN error model over other algorithmic methods that require *a priori* parameter specification (18; 24). Similarly, the BLN error model requires no specification of the gating or triggering thresholds used in physiologic methods.

This study had several limitations. First, the population statistically analyzed was small, homogeneous, and healthy. Results may not be generalizable to patients, and provide no information about focal or diffuse liver diseases. Second, the diffusion gradient direction was held constant, since liver is isotropic (4) and signal dropout is anisotropic according to previous studies (5; 28). Parameters reported here will not be comparable to parameters measured isotropically if there is any anisotropy in D, F or a. Third, BLN estimates were made using a single a for all b-values. There may in fact be a relation between a and b-value (see Appendix). Fourth, this work used relatively small matrix sizes and relatively large voxel sizes, to achieve a high signal-to-noise ratio that justifies comparison with the normal distribution instead of coil- and reconstruction-specific distributions. Matrix sizes for

diffusion-weighted echo planar imaging in the recent literature range widely, from 64 × 64 in a study of phase errors in single shot images of brain (23), to 80 × 80 and 120 × 256 in two different sequences in a study of IVIM parameters in liver tumors (30), to 144 × 192 as proposed in a review of liver diffusion imaging (1). Our study does not address the optimal matrix size for diffusion imaging, an important question given the low signal-to-noise ratio of small voxels in single shot imaging. Fifth, differences in diffusivity between the left and right liver lobes persisted even with the BLN error model, though they were smaller than with the LS error model. Work is required to investigate how these differences can be reduced further. Finally, our results show greater improvement in estimation of diffusivity than in estimation of perfusion fraction, likely for two reasons. First, our method mitigates signal dropout, which occurs at high b-values, while perfusion fraction is measured at low b-values. Second, our pulse sequence sampled relatively few low b-values, and may be inadequate for precise perfusion fraction estimation by either method.

Bulk motion causes stochastic signal dropout in diffusion images, as well as bias and variance in IVIM parameters derived from them. Maximum likelihood estimation of IVIM parameters under the BLN error model reduces bias and variance from bulk motion relative to LS estimates. Diffusion parameters from ungated, free-breathing protocols may have greater utility for diagnosis of liver diseases when estimated with the BLN error model.

Supplementary Material

Refer to Web version on PubMed Central for supplementary material.

Acknowledgments

The authors wish to acknowledge the financial support of GE Healthcare, salary support for Dr. Murphy from NIH Grant T32EB005970, and RSNA Grant RR1225.

References

1. Taouli B, Koh D-M. Diffusion-weighted MR imaging of the liver. Radiology. 2010; 254(1):47–66. [PubMed: 20032142]
2. Yablonskiy D, Sukstanskii AL. Theoretical models of the diffusion weighted MR signal. NMR in biomedicine. 2010 Aug; 23(7):661–81. [PubMed: 20886562]
3. Koh D-M, Collins DJ, Orton MR. Intravoxel incoherent motion in body diffusion-weighted MRI: reality and challenges. American Journal of Roentgenology. 2011 Jun; 196(6):1351–61. [PubMed: 21606299]
4. Taouli B, Dumont E, Daire J-luc, Fan B, Menu Y. Evaluation of Liver Diffusion Isotropy and Characterization of Focal Hepatic Lesions with MR Imaging Sequences: Prospective Study in 66 Patients. Radiology. 2003; 226(1):71–78. [PubMed: 12511671]
5. Murtz P, Flacke S, Traber F, van den Brink JS, Gieseke J, Schild HH. Diffusion-weighted MR Imaging with Pulse-triggered Single-Shot Sequences. Radiology. 2002; 224(1):258–264. [PubMed: 12091693]
6. Kwee TC, Takahara T, Niwa T, Ivancevic MK, Herigault G, Van Cauteren M, Luijten PR. Influence of cardiac motion on diffusion-weighted magnetic resonance imaging of the liver. MAGMA. 2009 Oct; 22(5):319–25. [PubMed: 19727877]
7. Kwee TC, Takahara T, Koh D-M, Nievelstein RaJ, Luijten PR. Comparison and reproducibility of ADC measurements in breathhold, respiratory triggered, and free-breathing diffusion-weighted MR

imaging of the liver. Journal of Magnetic Resonance Imaging. 2008 Nov; 28(5):1141–8. [PubMed: 18972355]

8. Kim SY, Lee SS, Byun JH, Park SH, Kim JK, Park B, Kim N, Lee M-G. Malignant hepatic tumors: Short term reproducibility of apparent diffusion coefficients with breath-hold and respiratory-triggered diffusion-weighted MR imaging. Radiology. 2010; 255(3):815–823. [PubMed: 20501719]
9. Kandpal H, Sharma R, Madhusudhan KS, Kapoor KS. Respiratory-triggered versus breath-hold diffusion-weighted MRI of liver lesions: comparison of image quality and apparent diffusion coefficient values. American Journal of Roentgenology. 2009 Apr; 192(4):915–22. [PubMed: 19304695]
10. Chandarana H, Taouli B. Diffusion and perfusion imaging of the liver. European Journal of Radiology. 2010 Dec; 76(3):348–58. [PubMed: 20399054]
11. LeBihan D. Intravoxel incoherent motion perfusion MR imaging: a wake-up call. Radiology. 2008 Dec; 249(3):748–52. [PubMed: 19011179]
12. LeBihan D, Breton E, Lallemand D, Aubin M-L, Vignaud J, Laval-Jeantet M. Separation of Diffusion and Perfusion in Intravoxel Incoherent Motion MR Imaging. Radiology. 1988; 168(2): 497–505. [PubMed: 3393671]
13. Moteki T, Horikoshi H. Evaluation of hepatic lesions and hepatic parenchyma using diffusion-weighted echo-planar MR with three values of gradient b-factor. Journal of Magnetic Resonance Imaging. 2006 Sep; 24(3):637–45. [PubMed: 16888790]
14. Bonekamp S, Torbenson MS, Kamel IR. Diffusion-weighted magnetic resonance imaging for the staging of liver fibrosis. Journal of Clinical Gastroenterology. 2011; 45(10):885–92. [PubMed: 21716125]
15. Yamada I, Aung W, Himeno Y, Nakagawa T, Shibuya H. Diffusion coefficients in abdominal organs and hepatic lesions: evaluation with intravoxel incoherent motion echo-planar MR imaging. Radiology. 1999 Mar; 210(3):617–23. [PubMed: 10207458]
16. Luciani A, Vignaud A, Cavet M, Nhieu JTV, Ruel L, Laurent A, Deux J-F, Brugieres P, Rahmouni A. Liver cirrhosis: Intravoxel incoherent motion MR imaging - Pilot study. Radiology. 2008; 249:891–899. [PubMed: 19011186]
17. Patel J, Sigmund EE, Rusinek H, Oei M, Babb JS, Taouli B. Diagnosis of cirrhosis with intravoxel incoherent motion diffusion MRI and dynamic contrast-enhanced MRI alone and in combination: preliminary experience. Journal of Magnetic Resonance Imaging. 2010 Mar; 31(3):589–600. [PubMed: 20187201]
18. Liau J, Lee J, Schroeder ME, Sirlin CB, Bydder M. Cardiac motion in diffusion-weighted MRI of the liver: artifact and a method of correction. Journal of Magnetic Resonance Imaging. 2012 Sep; 35(2):318–27. [PubMed: 21959926]
19. Taouli B, Sandberg A, Stemmer A, Parikh T, Wong S, Xu J, Lee VS. Diffusion-weighted imaging of the liver: comparison of navigator triggered and breathhold acquisitions. Journal of Magnetic Resonance Imaging. 2009 Sep; 30(3):561–8. [PubMed: 19711402]
20. Eatesam M, Noworolski SM, Tien PC, Nystrom M, Dodge JL, Merriman RB, Qayyum A. Liver diffusivity in healthy volunteers and patients with chronic liver disease: Comparison of breathhold and free-breathing techniques. Journal of Magnetic Resonance Imaging. 2011 Oct; 35(1):103–109. [PubMed: 22034200]
21. Taouli B, Sandberg A, Stemmer A, Parikh T, Wong S, Xu J, Lee VS. Diffusion-weighted imaging of the liver: Comparison of navigator triggered and breathhold acquisitions. Journal of Magnetic Resonance Imaging. 2011; 30(3):561–568. [PubMed: 19711402]
22. Dietrich O, Raya JG, Reeder SB, Ingrisch M, Reiser MF, Schoenberg SO. Influence of multichannel combination, parallel imaging and other reconstruction techniques on MRI noise characteristics. Magnetic Resonance Imaging. 2008 Jul; 26(6):754–62. [PubMed: 18440746]
23. O'Halloran RL, Holdsworth S, Aksoy M, Bammer R. Model for the correction of motion-induced phase errors in multishot diffusion-weighted-MRI of the head: Are cardiac-motion-induced phase errors reproducible from beat-to-beat? Magnetic Resonance in Medicine. 2011 Dec. (Epub ahead of print). 10.1002/mrm.23245
24. Pai VM, Rapacchi S, Kellman P, Croisille P, Wen H. PCATMIP: enhancing signal intensity in diffusion-weighted magnetic resonance imaging. Magnetic resonance in medicine: official journal

of the Society of Magnetic Resonance in Medicine/Society of Magnetic Resonance in Medicine. 2011 Jun; 65(6):1611–9.

25. Mwangi I, Hanna RF, Kased N, Malek P, Shiehmorteza M, Wolfson T, Gamst A, Sirlin C. Apparent diffusion coefficient of fibrosis and regenerative nodules in the cirrhotic liver at MRI. American Journal of Roentgenology. 2010 Jun; 194(6):1515–22. [PubMed: 20489091]
26. O'Neill R. Algorithm AS 47: Function Minimization Using a Simplex Procedure. Applied Statistics. 1971; 20(3):338–345.
27. Lee JT, Liau J, Murphy P, Schroeder ME, Sirlin CB, Bydder M. Cross-sectional investigation of correlation between hepatic steatosis and IVIM perfusion on MR imaging. Magnetic resonance imaging. 2012 May; 30(4):572–8. [PubMed: 22285877]
28. Nasu K, Kuroki Y, Fujii H, Minami M. Hepatic pseudo-anisotropy: a specific artifact in hepatic diffusion-weighted images obtained with respiratory triggering. MAGMA. 2007 Oct; 20(4):205–11. [PubMed: 17960439]
29. Castellares F, Montenegro LC, Cordeiro GM. The beta log-normal distribution. Journal of Statistical Computation and Simulation. 2011 Jul.10.1080/00949655.2011.599809
30. Wagner M, Doblas S, Daire JL, Paradis V, Haddad N, Leitão H, Garteiser P, Vilgrain V, Sinkus R, Van Beers BE. Diffusion-weighted MR Imaging for the Regional Characterization of Liver Tumors. Radiology. 2012 Aug.264:464–472.10.1148/radiol.12111530 [PubMed: 22692032]

Appendix

The mathematical tractability of the Beta*LogNormal error model allows three results. Note that we use a three-parameter version of this distribution, defined as the distribution of the product of independent Beta(α,1) and LogNormal(μ,σ^2) random variates, rather than the four parameter version given in (29).

First, the probability density function (PDF) of the Beta*LogNormal distribution can be expressed in closed form:

$$f_{BLN}(x;\alpha,\mu,\sigma^2)=\left(\frac{\alpha}{2}\cdot e^{\frac{\alpha}{2}(\alpha\sigma^2-2*\mu)}\right)\cdot\left(1-erf\left(\alpha\sigma^2-\mu+\frac{log(x)}{\sqrt{2\sigma^2}}\right)\right)\cdot x^{\alpha-1} \quad [A1]$$

A closed form PDF facilitates maximum likelihood parameter estimation. While we assign the second parameter of the Beta distribution to 1, we do not modify this assignment. Therefore, this approach is frequentist and not Bayesian. While this PDF involves the "error function" erf, implementations of erf are available on most computational platforms. Therefore, it is not a barrier to efficient maximum likelihood estimation. Method of moments estimators for α and σ^2 when μ=0 can be determined by solving the following set of equations, one of which is a quartic but is, again, not a barrier to efficient computational calculation:

$$\frac{1}{E^2(X)}\left(1+\frac{Var(X)}{E^2(X)}\right)=\frac{(\alpha+1)^4}{\alpha^3(\alpha+2)} \quad [A2]$$

$$E(X)=\left(\frac{\alpha}{\alpha+1}\right)\cdot e^{\frac{\sigma^2}{2}} \quad [A3]$$

Second, the Beta*LogNormal distribution can be related to bulk motion-induced phase errors, which are the mechanism behind the signal dropout artifact. Beta-distributed attenuation of signal magnitude over imaging time will arise from any distribution of intra-voxel phase errors (ϕ) for which the following relation holds:

$$|<e^{i\phi}>| \sim Beta(\alpha, 1) \quad \text{[A4]}$$

The bracket notation in [Eq A4] represents expectation value over the voxel, and the pipe notation indicates absolute value of the complex argument. A statistical distribution for phase error which satisfies this equation is:

$$\phi \sim WrappedNormal(\mu_\phi, 1) * Rayleigh\left(\sqrt{\frac{1}{\alpha}}\right) \quad \text{[A5]}$$

This relation implies that phase errors are normally distributed within the voxel, but are scaled by a Rayleigh-distributed random variate. Random scaling of the phase error arises because the velocity of bulk motion is, essentially, a random number whose value varies between images acquired at different points in time. This polar model of error better reflects the mechanism of signal dropout artifacts, since bulk motion leads to phase errors through [Eq 4]. Therefore, it is preferable to cartesian models of error that underlie least-squares fitting.

By [Eq. 4], phase from linear motion of spins is proportional to gradient strength and to velocity. For this to be true under [Eq. A5], the same proportionality must hold for the scale parameter of the Rayleigh random variate, since the wrapped normal variate is constrained by definition to [0,2π]:

$$\vec{G}_i \cdot \vec{v} \propto \sqrt{\frac{1}{\alpha_i}} \quad \text{[A6]}$$

This predicts the relation of α with b-value, since b-value is proportional to the square of gradient strength. Relative to α at b=1 s/mm^2, α_i at another b-value will be:

$$\alpha_i = \frac{\alpha}{b_i} \quad \text{[A7]}$$

That is, α_i should scale inversely with b-value. This may guide the choice of b-values to sample in a diffusion protocol, since $\alpha_i < 1$ results in a magnitude distribution whose mode is zero (Fig 3). In this work, we assumed a fixed α for all b-values, since there are mechanisms other than [Eq. 4] (such as the time-of-flight effect) which could cause stochastic magnitude attenuation but no relation between α_i and b-value. [Eq. A5] also predicts that:

$$v \propto \sqrt{\frac{1}{\alpha}} \quad [A8]$$

That is, $\alpha^{-½}$ is a measure of the distribution of the velocity of bulk motion in the direction of the gradient over imaging time. This result may allow quantification of "pseudo-anisotropy" (ie, signal dropout that depends on the gradient direction) that has been reported previously (28).

Third, the relation between Beta*LogNormal error and bias in diffusivity estimates can be calculated analytically. If Y_i is distributed according to [Eq. 5] with F=0, then the distribution of a simple estimator of diffusivity is as follows:

$$D_{est}=\frac{\sum logY_0-logY_i}{\sum b_i} \quad [A9]$$

$$D_{est}\sim Normal\left(D,\frac{\sigma^2}{n\cdot b_{avg}}\right)+\frac{1}{\sum b_i}Erlang(n,\alpha) \quad [A10]$$

$$E\left(D_{est}\right)=D+\frac{1}{\alpha\cdot b_{avg}} \quad [A11]$$

That is, D_{est} is an unbiased estimator of D in the presence of LogNormal error alone. However, in the presence of Beta error, D_{est} is biased by a number inversely proportional to α and the average b-value. Bias will always be positive since $\alpha > 0$ in the Beta distribution. Bias will be greater in locations with low α and in protocols that use low b-values to achieve short echo time for short T2 organs like liver. Similar bias is apparent in the relation of α with LS estimates of D (Fig 8).

In addition to these three benefits, the relation between this error model and the previously described p-means approach (18) can also be determined. If X is distributed as the product of a Beta random variate, reflecting signal dropout, and the correct value c, then the p-mean of X will approach the expectation value of X^p, which can be calculated analytically.

$$X\sim Beta(\alpha,1)\cdot c \quad [A12]$$

$$E(X^p)=\frac{\alpha}{\alpha+p}\cdot c^p \quad [A13]$$

For the p-mean algorithm to correct X to c, requires that this c be equivalent to the expectation value.

$$E(X^p)=c \quad \text{[A14]}$$

$$\frac{\alpha}{\alpha+p}\cdot c^p=c \quad \text{[A15]}$$

$$\frac{\alpha}{\alpha+p}\cdot c^{p-1}=1 \quad \text{[A16]}$$

This gives a relation between α, c and p. Although there is no closed form solution to this equation, it demonstrates that α and c determine the value of p that will correct a certain amount of signal dropout within a voxel. Since, α and c vary spatially, use of the same value for p in all voxels may be inappropriate.

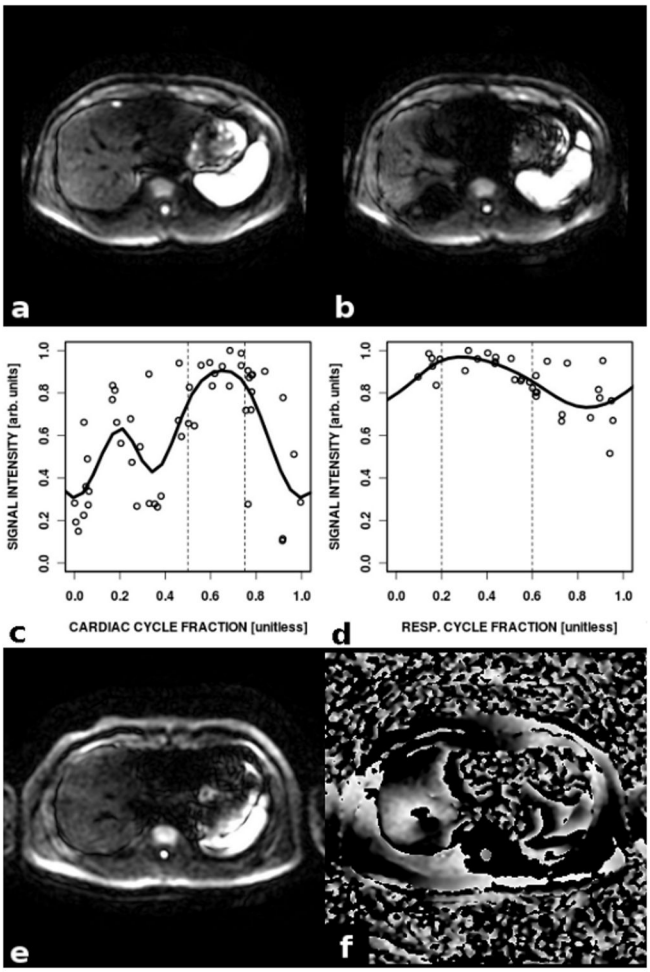

Figure 1. Signal dropout from bulk motion in DW-SE-EPI

Diffusion weighted images of liver are affected by signal dropout from bulk motion at specific times in the cardiac and respiratory cycles. In **(a, b)**, two single shot images acquired at the same b-value (b=500 s/mm2) and slice, but at different times in the scan, are shown. The entire left lobe of the liver, a portion of the right lobe, and most of a small focal lesion are greatly attenuated in **(b)** relative to **(a)**. In **(c, d)**, variation of signal intensity at a single b-value (b=500 s/mm2) is shown for an ROI in the left lobe **(c)** and for an ROI in the right lobe **(d)**. Signal intensity is plotted versus the time during the cardiac and respiratory cycles at which the image was acquired (defined as ratio of retrospective trigger delay to trigger interval, for peripheral pulse monitor and respiratory bellows monitor respectively). Trendlines (cyclic cubic splines through centroids of 7 bins) are shown (curves). Gating thresholds, within which signal was maximal and change was minimal, are indicated (vertical dashed lines, cardiac: 0.5–0.75, respiratory: 0.2–0.6). In **(e, f)**, magnitude and phase of a diffusion weighted image (b=500 s/mm2) are shown. There is rapid change in phase **(f)** as the region of signal dropout in the left lobe is approached **(e)**. This suggests a mechanism of attenuation other than diffusion, which causes no net phase.

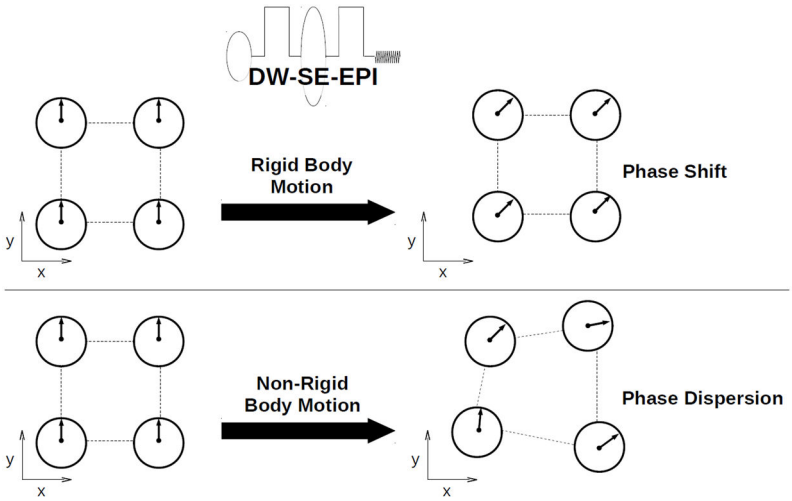

Figure 2. Phase dispersion induced by non-rigid body motion

During a bipolar gradient, the phase of a spin within a voxel is shifted by motion according to [Eq 4]. If the voxel does not move as a rigid body, spins in different locations within the voxel will experience different phase shifts, leading to phase dispersion. Magnitude attenuation from this mechanism will occur in addition to that from diffusion. The Beta*LogNormal distribution models attenuation from bulk motion and attenuation from diffusion separately.

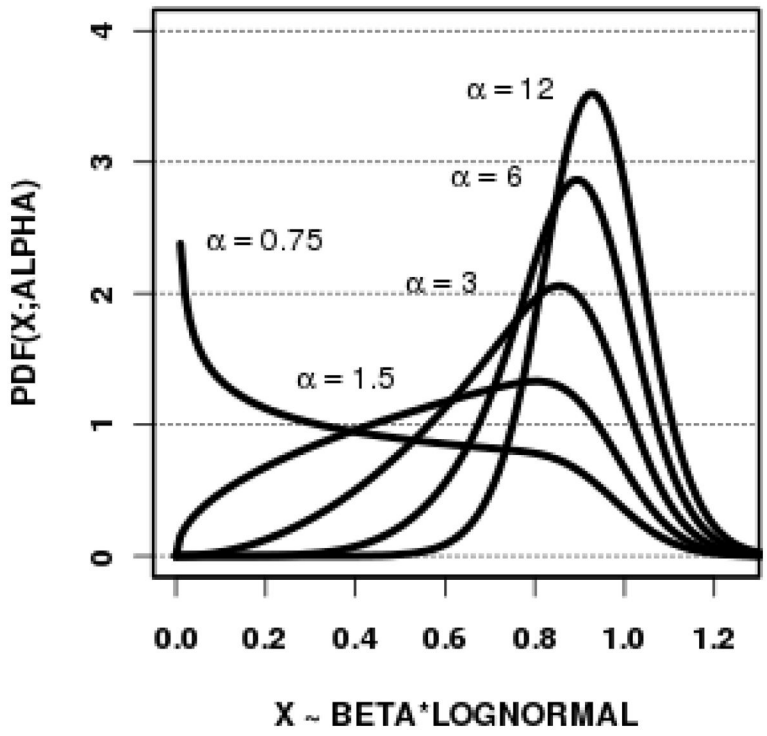

Figure 3. The Beta*LogNormal distribution

The probability density function of the Beta*LogNormal distribution is shown for increasing values of α, at constant $\exp(\mu)=1$ and $\sigma^2=0.01$. Lower α produces negative skewness relative to $\exp(\mu)$, reflecting signal dropout. Higher α produces a distribution similar to other signal magnitude distributions.

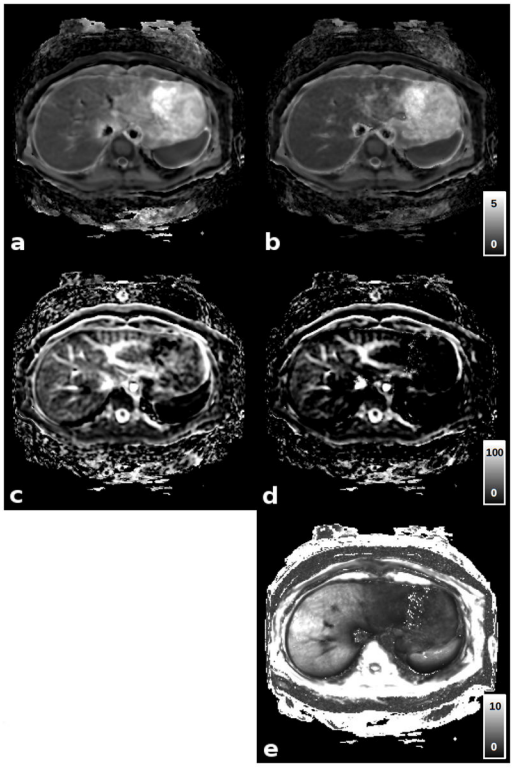

Figure 4. IVIM parameter maps

Typical parametric maps of D **(a, b)** and F **(c, d)** from the LS **(a, c)** and BLN **(b, d)** error models derived from images from an ungated scan of a volunteer are shown at matrix size 92×92. Diffusivities in the left lobe of the liver are appreciably greater in **(a)** than **(b)**. Map of α from the BLN error model is shown as well **(e)**. Low α indicates areas of high stochastic signal dropout. Units for gray-scale bars are 1E-3 mm^2/s **(a, b),** [%] **(c, d)**, and unitless **(e)**.

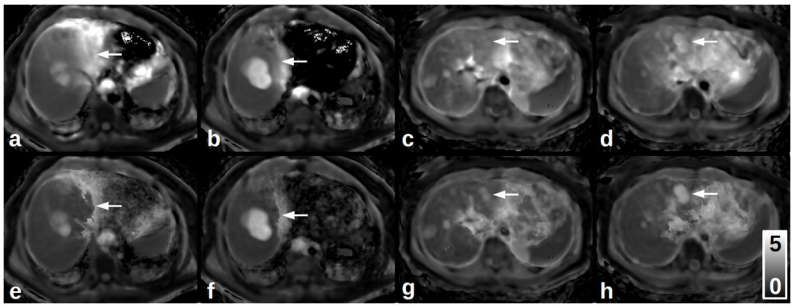

Figure 5. Diffusivity maps in two patients with focal liver lesions

LS **(a, b, c, d)** and BLN **(e, f, g, h)** error models were used to generate parametric maps of D without gating in two patients with focal liver lesions. Two contiguous slices are shown for each patient. The first patient **(a, b, e, f)** had a 5 cm cyst in the right liver lobe. The second patient **(c, d, g, h)** had multiple lesions, including two 1 cm cysts in the left liver lobe. In the LS maps, diffusivity is artifactually elevated in the liver parenchyma to the left of each lesion (arrows), reducing contrast between lesion and parenchyma, and potentially leading to incorrect classification of the lesion as benign or malignant. This effect occurs because of signal dropout from cardiac motion, and is mitigated in the BLN maps. Window and level settings are the same for all images. Units for gray-scale bars are 1E-3 mm^2/s.

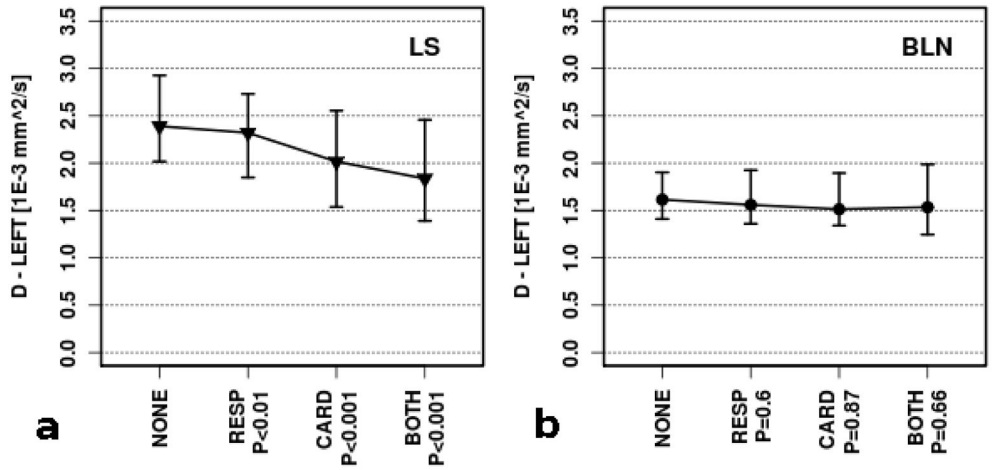

Figure 6. Gating-dependent changes in D

Estimates of D in the left lobe of the liver of six subjects were derived with the LS **(a)** and BLN **(b)** error models using four varieties of gating: (ungated: NONE, respiratory gated: RESP, cardiac gated: CARD, cardiac and respiratory gated: BOTH). Median and 25–75% quantiles are shown. LS estimates changed significantly ($P<0.01$) as a function of gating, indicating bias from bulk motion at specific phases of the cardiac and respiratory cycles. BLN estimates did not change significantly as a function of gating ($P>0.1$). Since absence of significant differences can be due to increased variance rather than closer means, further tests were performed to exclude that possibility.

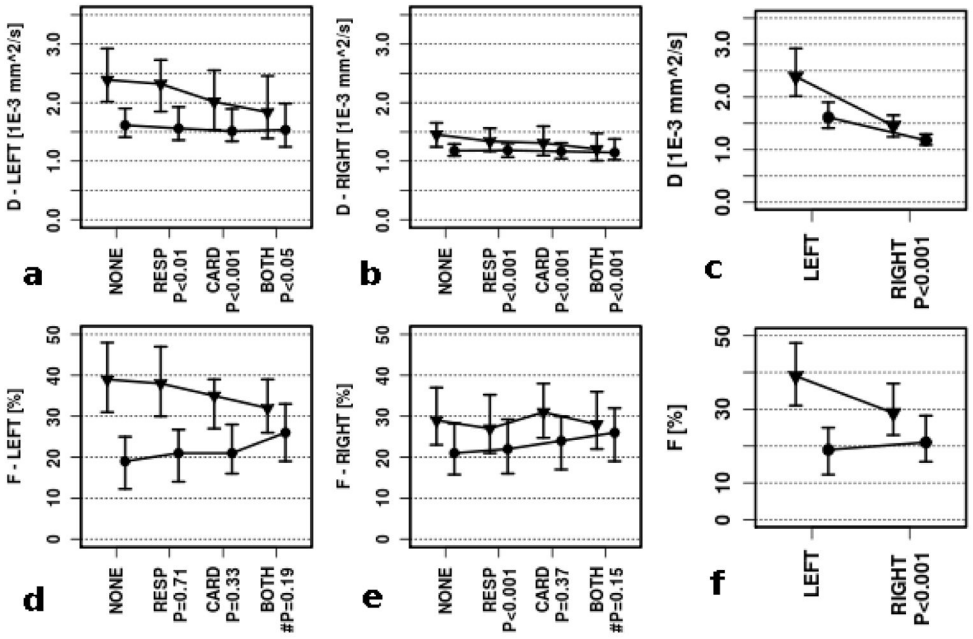

Figure 7. Gating- and lobe-dependent changes in IVIM parameters

Estimates of D **(a–c)** and F **(d–f)** in parametric maps derived from LS (triangle) and BLN (circle) error models were measured in multiple ROI's colocalized across four gating variants **(a, b, d, e)** in the left **(a, d)** and right lobes **(b, e)** of the liver. The ungated left and right lobe estimates are shown in (c, f). Median and 25–75% quantiles are shown. P-values are shown for the hypothesis that BLN estimates changed less than LS estimates as a function of gating or lobe. P-values annotated with (#) support the opposite hypothesis. Gating- and lobe-dependent changes in D and lobe-dependent changes in F were significantly lower for BLN estimates than for LS estimates ($P<0.05$).

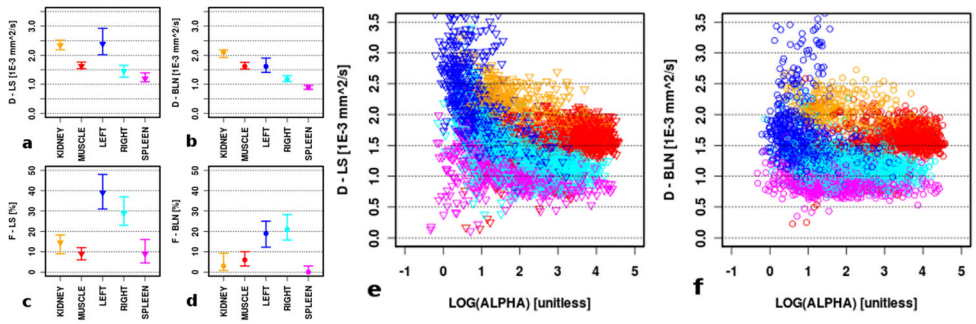

Figure 8. IVIM parameters as a function of organ type

Estimates of D **(a, b)** and F **(c, d)** derived from the LS **(a, c)** and BLN **(b, d)** error models were measured without gating in multiple ROI's in liver, spleen, kidney, and paraspinous muscles of the back. Median and 25–75% quantiles are shown above. There were significant differences between the right lobe of the liver and each other organ type, including the left lobe, for both parameters from both error models ($P<0.01$, except for one case). The variance of D was significantly lower for BLN estimates than LS estimates for each organ type ($P<0.05$), except for the left lobe of liver ($P=0.12$) and for muscle ($P=0.61$). Variance of D was reduced in the left lobe of the liver, but not by a statistically significant amount. Estimates of D from the LS **(e)** and BLN **(f)** error models are plotted as a function of α for ROI's in each organ type (right liver lobe: blue, left liver lobe: cyan, spleen: magenta, kidney: orange, muscle: red). Every variety of gating for three voxel size variant scans is included. In liver, an inverse relationship between D and α, similar to that predicted by [Eq. A11], can be appreciated for LS estimates, which is reduced though not eliminated for BLN estimates.